SUPPORTING INFORMATION FOR:

Diameter-dependent optical absorption and excitation energy transfer from encapsulated dye molecules towards single wall carbon nanotubes

Stein van Bezouw,[†,#] *Dylan H. Arias,*[‡,#] *Rachelle Ihly,*[‡] *Sofie Cambré,*[†] *Andrew J. Ferguson,*[‡] *Jochen Campo,*[†] *Justin C. Johnson,*[‡] *Joeri Defillet,*[†] *Wim Wenseleers**[†] *and Jeffrey L. Blackburn**[‡]

[†]Physics Department, University of Antwerp, Universiteitsplein 1, B-2610 Antwerp, Belgium
[‡]National Renewable Energy Laboratory, Golden, Colorado 80401, United States

[#]These authors contributed equally.
*Corresponding authors: wim.wenseleers@uantwerp.be, jeffrey.blackburn@nrel.gov,

Table of Contents

1. Thermogravimetric analysis

Thermogravimetric analysis (TGA) was performed on a Mettler Toledo TGA/SDTA851e thermobalance. Samples were heated from room temperature up to 800°C at a rate of 1°C/min in air. Figure S1 represents the TGA and derivative TGA (DTGA) curves of the AD and LV950 SWCNTs. The AD SWCNT powders decompose in two main steps, the first one (at about 350°C, weight fraction of 54.8%) corresponding to the oxidation of amorphous carbon and the second DTGA peak (at about 550°C, weight fraction 22.3%) is corresponding to the SWCNTs. The TGA curves furthermore show about 22.9% of non-combustible material, i.e. metallic catalyst particles and their oxides. Hence, based on these TGA results oxidation was performed at 460°C for several hours until a weight loss of 55% was obtained. The LV950 SWCNTs only show one oxidation peak (at about 340°C), hence a gentler oxidation was applied, burning only 18% of the material at 300°C. In this case, the remaining sample still contains about 32% of non-combustible catalytic nanoparticles.

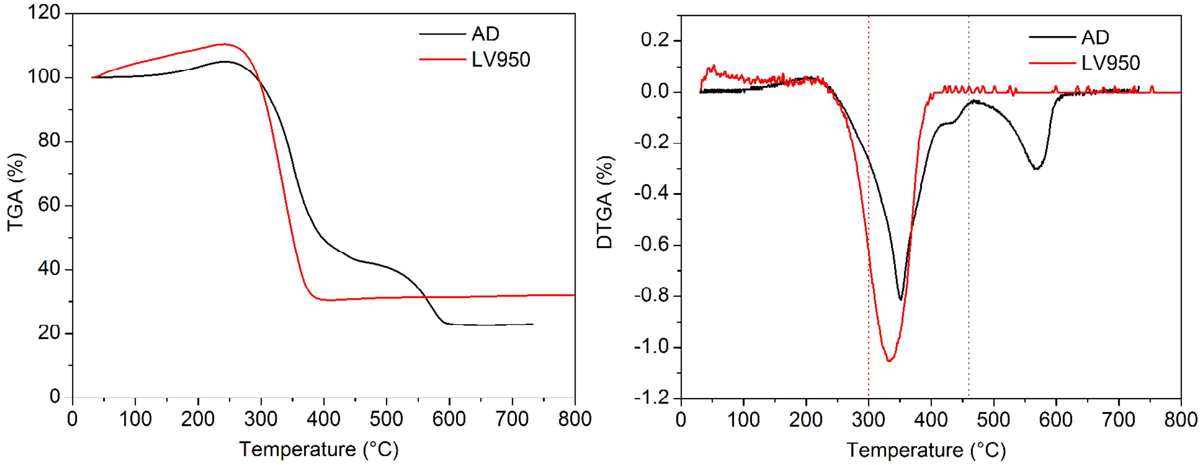

Figure S1: Thermogravimetric analysis of raw SWCNT powder. (left) TGA curves of AD (black) and LV950 (red) SWCNTs. (right) Corresponding derivative-TGA (DTGA) curves with dashed lines indicating the oxidation temperature.

2. Additional Absorption Spectra

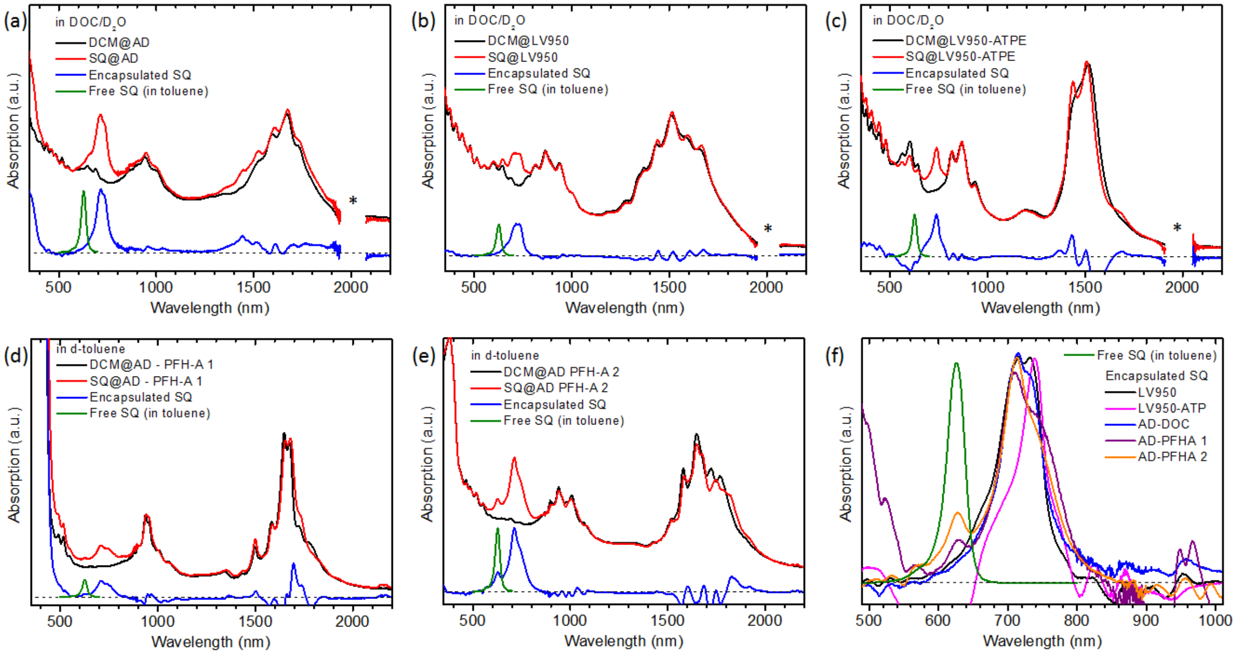

Figure S2: Absorption spectra of SQ@SWCNTs (a-e) Normalized absorption spectra of SQ@SWCNT (red) and DCM@SWCNT (black), encapsulated SQ absorption (blue) obtained by subtracting the spectra of SQ@SWCNT – DCM@SWCNT and comparison with SQ dissolved in toluene (green). The absorption spectra are not shown in the region indicated by *, as D_2O absorbs too strongly in this region to allow reliable absorption measurements for the cell path length used. (a) AD SWCNTs in DOC/D_2O, (b) LV950 SWCNTs in DOC/D_2O, (c) ATPE sorted LV950 SWCNTs, (d) AD in PFH-A/d-toluene (low molecular weight) and (e) AD in PFH-A/d-toluene (high molecular weight). (f) Normalized absorption spectra of SQ in toluene and encapsulated SQ obtained from the different SWCNT batches and different solubilization methods (DOC- or polymer-wrapped SWCNTs; see legends) and hence different diameter distributions.

3. Closed SWCNT reference sample

To further prove the encapsulation, a closed SWCNT reference sample was prepared. Raw LV950 SWCNTs were opened only partially by skipping the oxidation step and hence only sonicating the sample in concentrated HCl followed by rinsing with deionized water and vacuum annealing at 800°C. Apart from the absence of oxidation, this SWCNT batch was treated in the same way as the other samples to ‘fill’ the SWCNTs, but now only the fraction of opened SWCNTs can be filled. Afterwards the samples were dispersed in 1% wt/V DOC/D_2O and separated by density gradient ultracentrifugation. The closed SWCNTs in this sample have a much lower density than the opened, filled SWCNTs and can thus be found at a different height in the density gradient within the centrifuge tube (see Figure S3a). The absorption spectrum of this empty fraction clearly demonstrates that no dye absorption is present. This demonstrates that the applied rinsing procedure thoroughly removes the excess dye molecules adsorbed on the outer walls of the CNTs but leaves the molecules in the interior hollow core of the SWCNTs in place in the SQ@SWCNT samples.

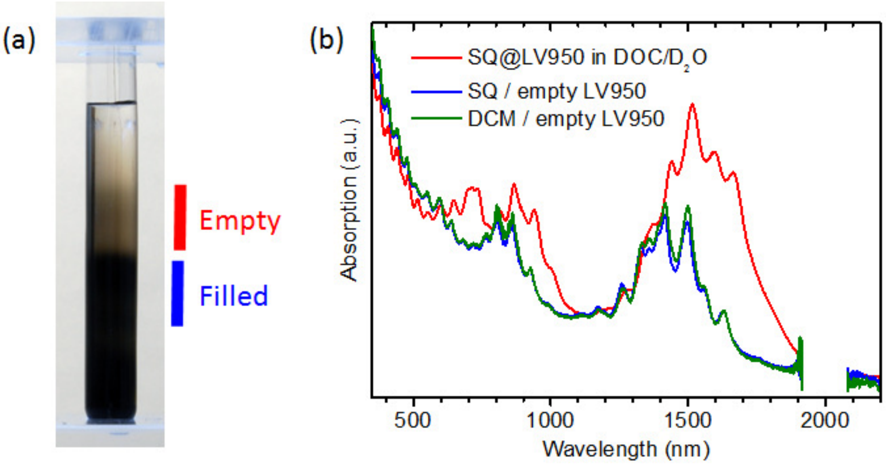

Figure S3: Reference sample with empty SWCNTs. (a) DGU centrifuge tube of partially opened LV950 SWCNTs, indicating the empty/closed (lower density) and the filled/opened SWCNT (higher density) fractions. (b) Absorption spectra of the empty SWCNT fractions for the SQ-treated LV950 SWCNTs (blue) and the DCM-treated LV950 SWCNTs (green). For comparison also the SQ-filled LV950 absorption spectrum is presented (red). Empty fractions clearly have no dye absorption whatsoever present in the sample, and do not show the red-shift observed for the SQ-filled SWCNTs.

4. <u>Postdispersion filling</u>

The fact that for the polymer-dispersed filled SWCNTs (SQ@AD-PFHA1 and SQ@AD-PFHA2) a small fraction of the encapsulated molecules exits the SWCNTs and redisperses into the toluene suspension, opens the interesting possibility to reverse this process and perform the SQ encapsulation after the polymer dispersion. To this end a batch of opened AD SWCNTs was first dispersed using PFHA1 in toluene. This solution was subsequently saturated by adding SQ powder, and its linear absorption spectrum was monitored as a function of duration of bath sonication. An absorption band associated with encapsulated SQ (at about 710nm) was indeed observed, with increasing intensity proportional to sonication time. It is intriguing that both filling methods (before dispersion as presented in the main manuscript or after dispersion as presented here) yield very similar relative intensities of the encapsulated SQ molecules with respect to the SWCNTs (Figure S4), but that the most strongly red-shifted absorption contributions (corresponding to the thinnest SWCNT diameters as derived from the PLE analysis) are not observed in the postdispersion filling case. We believe that for these thinnest

SWCNTs, in which the SQ molecules barely fit, the polymer wrapping prevents the dyes to enter the SWCNTs.

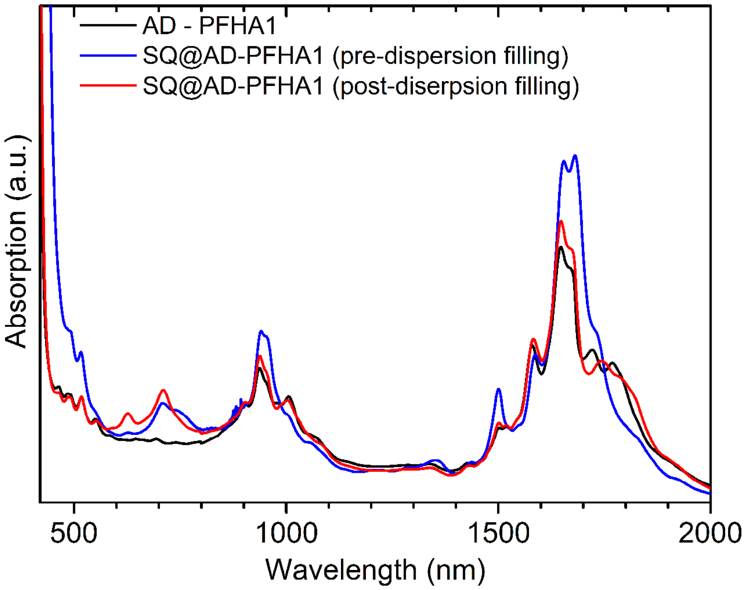

Figure S4: Postdispersion filling of AD SWCNTs. (black) Absorption spectrum of pre-opened AD SWCNTs dispersed by PFHA1 in toluene; (blue) Absorption spectrum of SQ@AD-PFHA1 prepared by first filling the AD SWCNTs (by the refluxing process as described in the main text) and afterwards dispersing the filled SWCNTs with the same polymer and (red) Absorption spectrum of SQ@AD-PFHA1 prepared by first dispersing the opened AD SWCNTs and afterwards filling them by adding SQ to the suspension and applying 5 hours of bath sonication (postdispersion filling).

5. Quenching of the SQ fluorescence upon SWCNT encapsulation

The high efficiency of the energy transfer is illustrated by essentially complete quenching of the fluorescence of the encapsulated SQ molecules, while SQ is known to be strongly fluorescent otherwise (QY of 0.85 in toluene[1]). To estimate the quenching factor, we measured the fluorescence of SQ dissolved in toluene (excited at the high-energy side of the absorption maximum; 610nm) and compared this to the fluorescence of the SQ molecules in the SQ@AD-DOC sample (excited at 690nm, *i.e.* at the high-energy side of the absorption band associated with the encapsulated SQ). Samples were diluted (optical density about 0.05 in a 1 cm path length fused silica cell) to minimize effects of reabsorption. This results in a reduction of the SQ fluorescence efficiency for SQ@AD-DOC by a factor of ~100,000 with respect to SQ in toluene. It should be noted that this value, though already very high, still represents a lower bound to the actual quenching factor, as no clear fluorescence signal is detected. To get the most conservative estimate of the quenching factor, the very weak background signal observed for the SQ@AD-DOC sample is included in the (integrated) fluorescence, while this signal does not resemble the fluorescence spectrum of SQ at all, and in fact a very similar background was observed for the

DCM@AD-DOC reference sample. Interestingly, also upon excitation of the SQ@AD-DOC sample at the $\lambda_{\max}$ of the free dye, no fluorescence attributable to the free dye could be detected, demonstrating that not even trace amounts of the free dye are present in the SQ@AD-DOC sample.

6. Resonant Raman spectroscopy of SQ-filled SWCNTs

We collected Raman spectra of the encapsulated dye molecules in the SQ@LV950-DOC sample at 5 different excitation wavelengths (Fig. S5), both resonant and non-resonant with the dye absorption. For comparison, measurements for the DCM-filled reference sample, as well as for the pure SQ powder and for a solution of SQ in DCM were obtained. Due to strong fluorescence from the SQ powder and solution, which results in overly strong backgrounds in the Raman spectra, it was only possible to obtain a Raman spectrum of the SQ powder at short excitation wavelength, i.e. 514.5nm, while the SQ solution did not yield measurable Raman intensity from the SQ dye at any of the chosen wavelengths.

Thanks to the strong quenching of the dye emission after encapsulation, it is possible to measure Raman spectra (even) with laser wavelengths scanning all the way through resonance with the dye absorption. At 514.5nm, far from resonance, the dye cannot be observed, and the Raman spectrum is completely dominated by the SWCNT vibrations. Note also that no difference in the G-band spectrum can be observed, indicating that the SWCNTs are not doped by the encapsulation of the dye. Tuning to longer wavelengths, first the higher-frequency SQ Raman modes (i.e. ~1570cm^{-1}) come in resonance. This can be understood as e.g. for λ_{exc} = 647.1 nm, the incident photon is still out of resonance, but the outgoing (Stokes-shifted) photons for vibrational frequencies >1000cm^{-1} are in resonance with the encapsulated dye absorption band at ~700-780nm). At longer wavelengths (λ_{exc} = 676.4 nm), the intermediate frequencies (~500-1200cm^{-1}) become resonant and when the incoming laser wavelength itself approaches the resonance with the dye absorption (especially at λ_{exc} = 712 and 738nm), also a low frequency Raman mode of the dye (178 cm^{-1}, highlighted by the vertical dotted line in Figure S5), corresponding to a SQ ring-vibration is strongly enhanced. The strong resonant enhancement of this SQ ring-vibration mode makes it very difficult to monitor the radial breathing modes (RBMs) of the SWCNTs, and their possible filling-induced vibrational shifts, for excitation throughout the dye resonance, as the intensity of the low-frequency dye vibration overwhelms the RBMs. At (incoming) resonance, we also observe an increasing background at low frequency, which could originate from a small contribution of hot fluorescence from the encapsulated dye molecules.

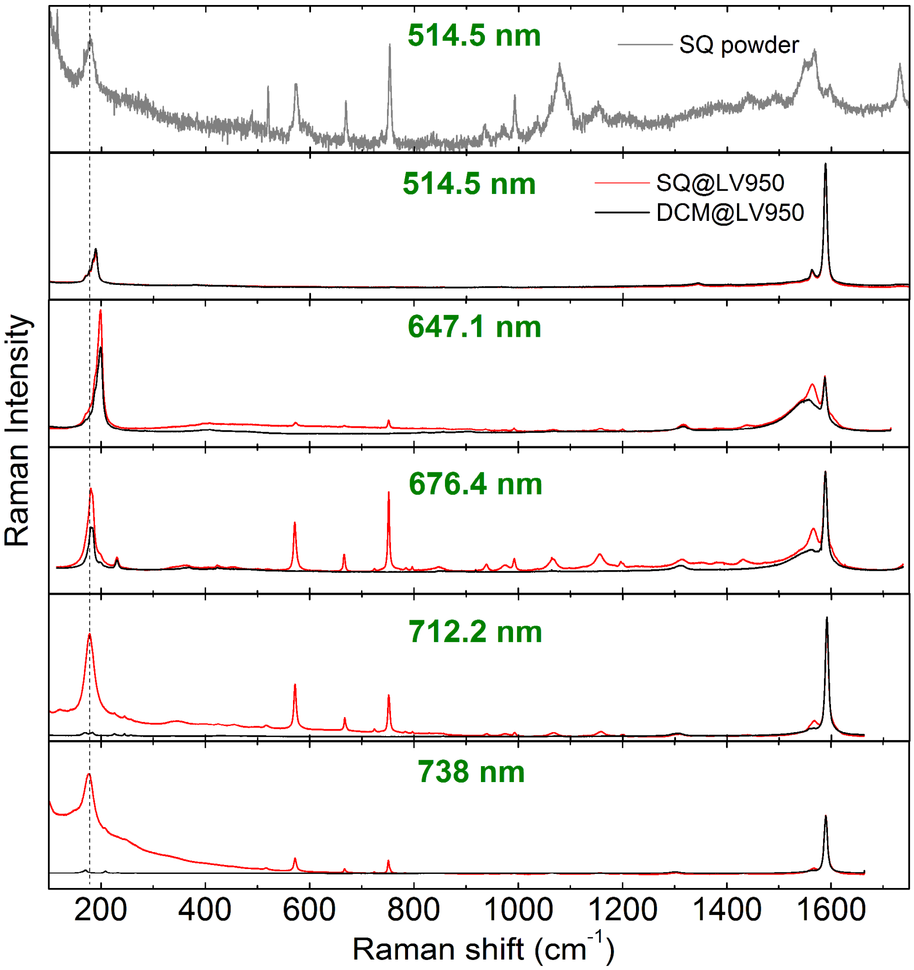

Figure S5: RRS spectra of the SQ powder (grey), SQ@LV950 (red) and DCM@LV950 (black) SWCNT samples as a function of excitation wavelength. Spectra are normalized on the G-band vibrational frequency of the SWCNTs. The dashed vertical line marks the SQ ring vibration which strongly overlaps with (and overwhelms when at resonance with the dye absorption) the SWCNT RBM modes (in the range of 170-300cm^{-1} as observed in the reference sample).

To overcome the strong resonance enhancement of this SQ ring-vibration mode, we measured changes of the radial breathing modes of the SWCNTs by excitation at 810 nm and 864 nm (Figure S6). These data show clear shifts of the RBM peak positions for the SQ-filled SWCNTs with respect to the DCM-filled SWCNTs, in particular for larger-diameter SWCNTs, e.g. the (11,6) and (12,5) chirality, which can be attributed to the filling with SQ dye molecules as opposed to filling with DCM in the reference sample, as previously observed for other filler molecules.[2]

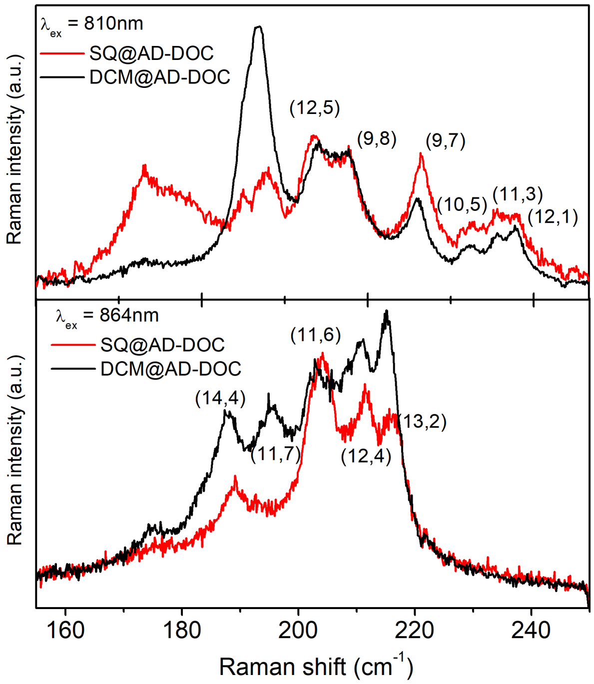

Figure S6: Representative RBM Raman spectra of the SQ@AD-DOC (red) and DCM@AD-DOC (black) samples, measured at two different excitation wavelengths. Clear shifts of the RBM peak positions can be observed for the larger-diameter SWCNTs, such as the (11,6) and (12,5) SWCNTs indicative of filling with the SQ dye molecules.[2]

7. Additional PLE data.

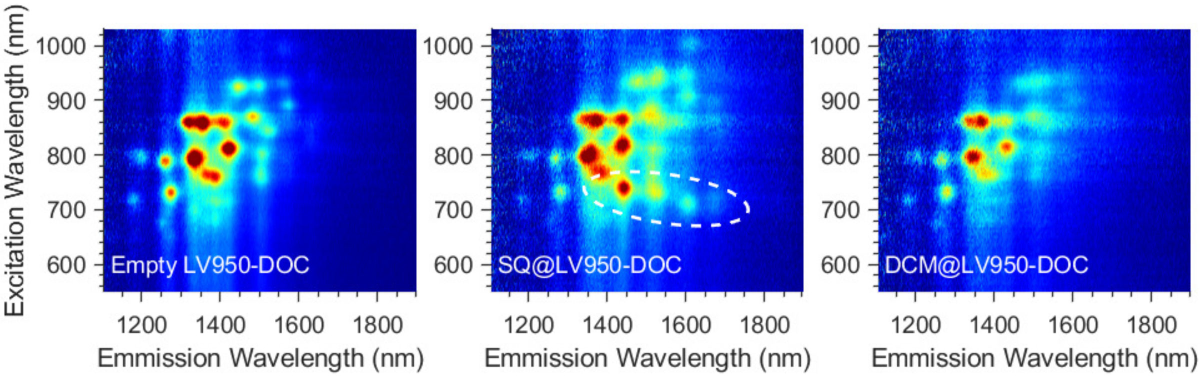

Figure S7: PLE maps of empty, SQ-filled and DCM-filled LV950 SWCNTs in DOC/D_2O. The white dashed ellipse highlights the EET peaks.

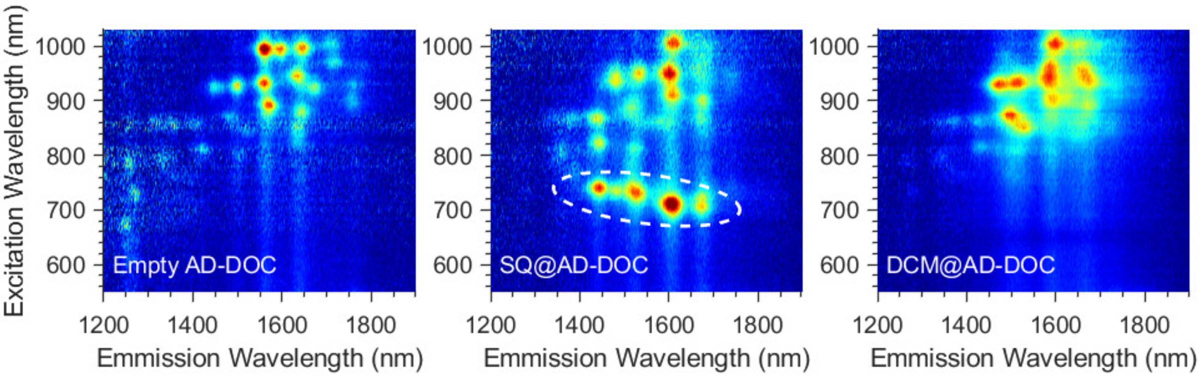

Figure S8: PLE maps of empty, SQ-filled and DCM-filled AD SWCNTs in DOC/D_2O. The white dashed ellipse highlights the EET peaks.

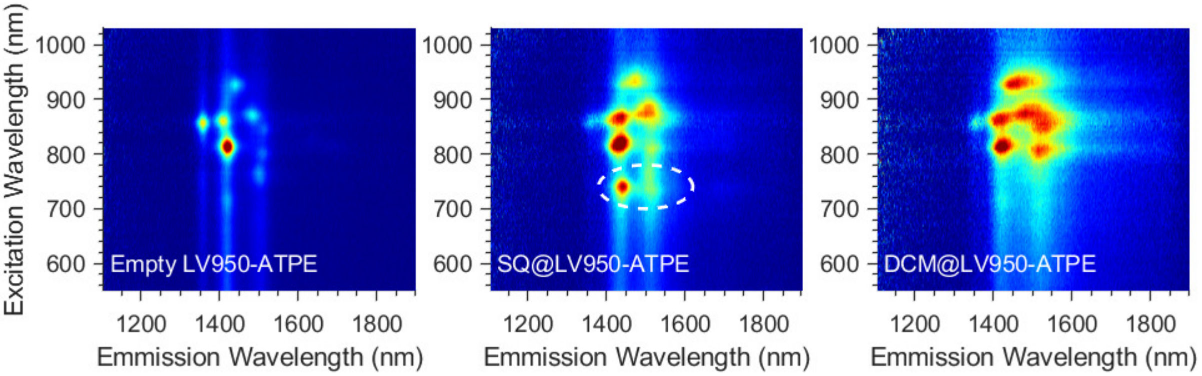

Figure S9: PLE maps of empty, SQ-filled and DCM-filled ATPE-sorted LV950 SWCNTs in DOC/D_2O. The white dashed ellipse highlights the EET peaks.

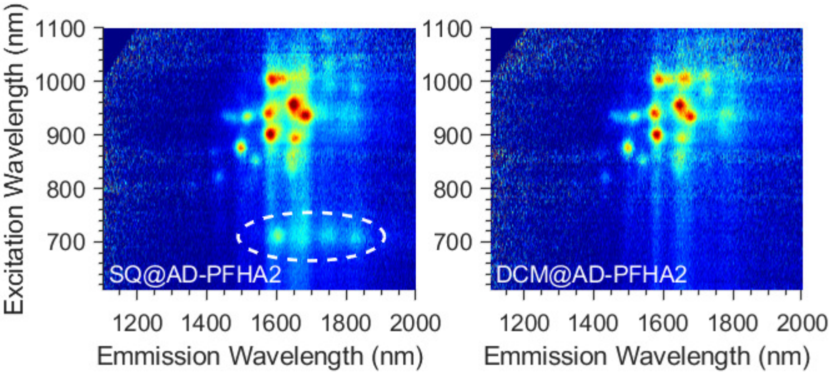

Figure S10: PLE maps of SQ-filled and DCM-filled AD SWCNTs, wrapped with PFH-A2 in deuterated toluene. The white dashed ellipse highlights the EET peaks.

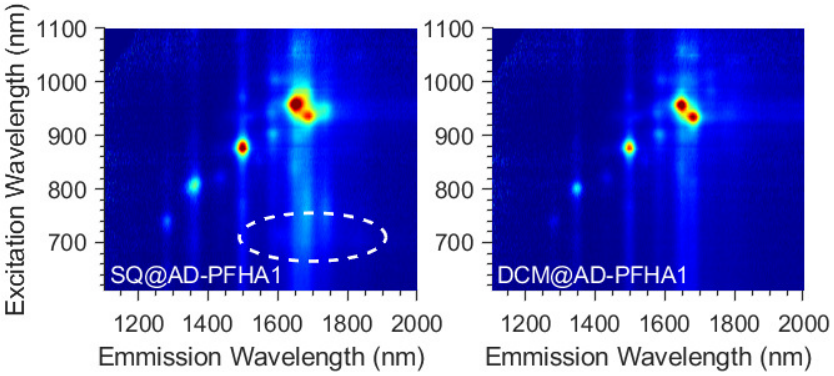

Figure S11: PLE maps of SQ-filled and DCM-filled AD SWCNTS, wrapped with PFH-A1 in deuterated toluene – near armchair SWCNTs. The white dashed ellipse highlights the EET peaks.

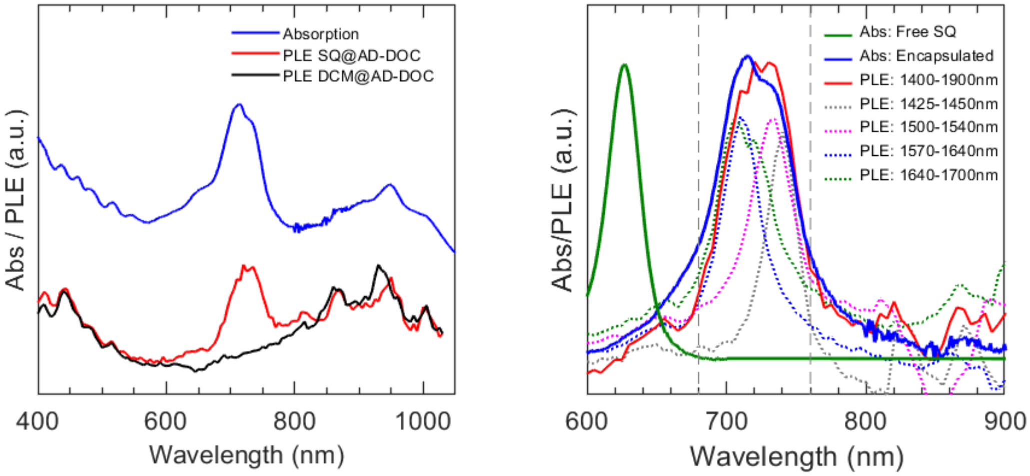

Figure S12: Comparison of the SQ absorption band in absorption and PL excitation spectra. (left) Comparison of the absorption spectrum of the SQ@AD-DOC sample (blue) and corresponding integrated PL excitation over the complete emission wavelength range from 1400-1900nm for the SQ@AD-DOC sample (red) and the reference DCM@AD-DOC sample (black). (right) Absorption spectrum of the freely dissolved SQ molecules in toluene (solid green), and difference absorption spectrum of encapsulated SQ molecules inside AD SWCNTs (i.e. absorption spectrum of SQ@AD-DOC minus that of DCM@AD-DOC, solid blue). PL excitation spectra of SQ@AD-DOC obtained by integrating between the indicated wavelength ranges (corresponding to more narrow sets of chiralities) and subtracting the corresponding DCM@AD-DOC spectrum (dotted curves). The overlapping full excitation spectrum (solid red; i.e. difference between red and black curve in the left panel) obtained by integrating over the complete emission range corresponds very well to the difference absorption spectrum.

8. Subtraction of Normalized PLE maps.

For comparison of EET peaks and relative intensities, we perform a normalization and subsequent subtraction of the PLE maps of SQ- and DCM-filled samples (Figure 2f in main text). When looking at the EET bands in the PLE maps, it is important to note that the intensity of the EET band depends strongly on the abundance (and PL efficiency) of the SWCNTs present in the different samples. The intensity of the EET band is thus modulated by the abundance of the SWCNTs for each specific emission wavelength and the abundance of the SWCNTs varies dramatically between the different samples. To account for both effects, it is useful to normalize the PLE map of the SQ@AD-DOC sample for each emission wavelength over the intrinsic S_{22} excitation intensity of the SWCNTs, as was done previously for other dye-filled SWCNTs.[2] After normalization of the SQ@AD-DOC and DCM@AD-DOC samples, we subtracted both normalized PLE maps to end up with the SQ EET bands, normalized on the intrinsic SWCNT signals.

9. SQ solvatochromism

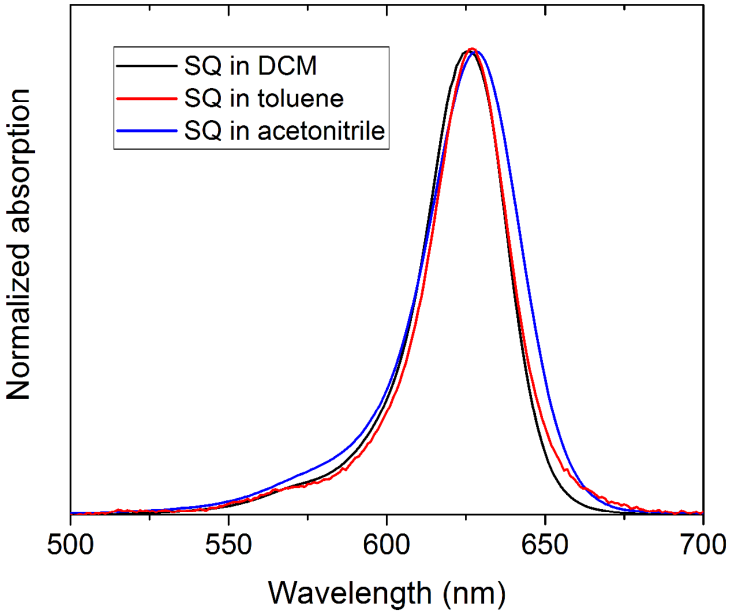

Figure S13: Solvatochromic behavior of free SQ in solution. Absorption spectra of SQ dissolved in different solvents with very different polarity showing just a minor change in peak absorption wavelength (dielectric constants: toluene: 2.38, DCM: 8.93, and acetonitrile: 37).

10. Two-dimensional fits of the PLE maps

The empirical fitting model that was used to fit the PLE maps was based on the previous fitting procedure described in the supporting information of reference [2]. The model was slightly optimized, and the excitation profiles were adapted to also include the EET peaks.

The basic model comprises:

(a) For each chirality an emission peak is included as a Voigt line shape, with transition energy E_{11}, full-width-at-half-maximum $FWHM_{11}$ and a shape parameter describing the relative width of Lorentzian and Gaussian contributions to the line shape.

(b) For each chirality an excitation profile is devised, including both excitonic and band-to-band absorptions:

   i. E_{22} excitonic absorption is fitted using a Voigt lineshape with transition energy E_{22}, linewidth $FWHM_{22}$ and a shape parameter as above (the value of the E_{22} and E_{11} shape parameters are different).

   ii. Band-to-band absorptions are modeled as $\sim 1/\sqrt{\mathrm{E} - E_{22}}$ and convoluted with a Gaussian line shape with width $FWHM_{22}$, obtained from the excitonic absorption spectrum. Similarly, a band-to-band absorption related to the first optical transition E_{11} is included, only the high energy tail of which is used to account for absorption at longer wavelengths than the E_{22} excitonic absorption. The amplitude of the band-to-band absorption contribution is fitted as a relative value with respect to the amplitude of the corresponding E_{22} excitonic transitions and is taken the same for all chiralities.

   iii. A phonon side band, residing at approx. 0.2eV above the E_{22} excitation is also included. The precise position is fitted, but taken the same for all the SWCNT chiralities, and the line shape and width are taken the same as for the excitonic E_{22} contribution. To account for the differences in electron-phonon coupling for different SWCNTs, a diameter-dependent amplitude of this phonon side band, A_{ph}, was included in the fit, in the form of $A_{ph} = A.d^{-\alpha}$, with A and α fitting parameters. The amplitude A, is again fitted as a relative value with respect to the amplitude of the corresponding E_{22} excitonic transitions and is taken the same for all chiralities.

   iv. Finally, for the SQ-filled SWCNTs we use the absorption spectrum of the SQ dye in toluene as a starting profile for the encapsulated dye absorption spectra (i.e. EET excitation profiles) which is shifted and scaled (in energy space). For each chirality, the peak position and relative amplitude versus the E_{22} excitonic absorption is fitted separately (to account for different filling fractions which was found to be necessary to obtain a good fit), while the line width of the absorption peak is taken the same for all chiral structures.

(c) Finally, the so-obtained emission and excitation profiles are combined in a 2D fitting function for each chiral structure – of which the E_{22} excitonic transition amplitudes are determined by a simple (analytical) linear regression. As such these amplitudes do not require numerical optimization.

To obtain the SWCNT peak positions over a broad diameter range, the AD, LV950 and polymer-wrapped samples needed their own set of intrinsic SWCNT emission and excitation peaks (due to the different external environment and different filling fractions in the respective samples). However, the EET excitation peak positions are not noticeably influenced by the external environment or filling fractions, hence these were fitted simultaneously for all samples. As such, the different SWCNT abundances in different samples allow for a more reliable extraction of the EET peak positions for the SQ dye encapsulated inside different SWCNTs.

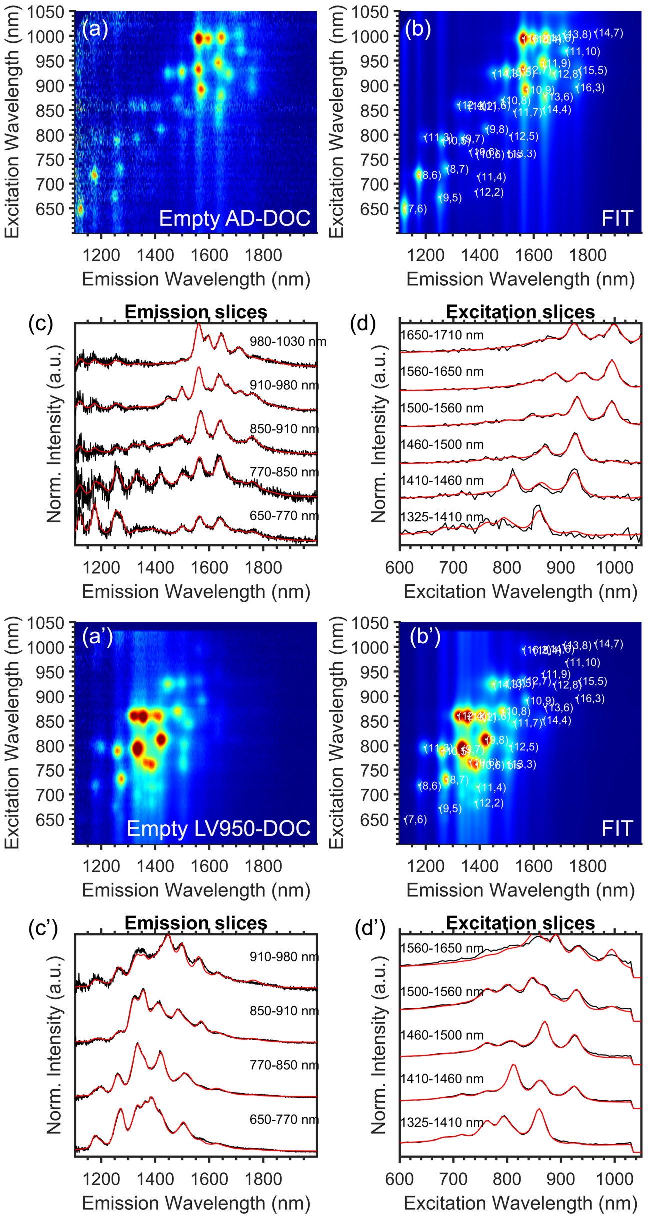

Figure S14: Experimental PLE maps and fits of empty AD (top 4 panels) and empty LV950 (bottom 4 panels) samples, fitted simultaneously with equal peak positions and line widths and varying amplitudes for each of the SWCNT peaks. Experimental (a, a') and fitted (b, b') PLE maps are presented, with fitted peak positions indicated by white dots and associated chiral indices. Integrated emission (c, c') and excitation (d, d') spectra of experimental (black) and fitted (red) PLE maps, integrated over the indicated wavelength ranges, highlight the excellent correspondence between experimental data and fit.

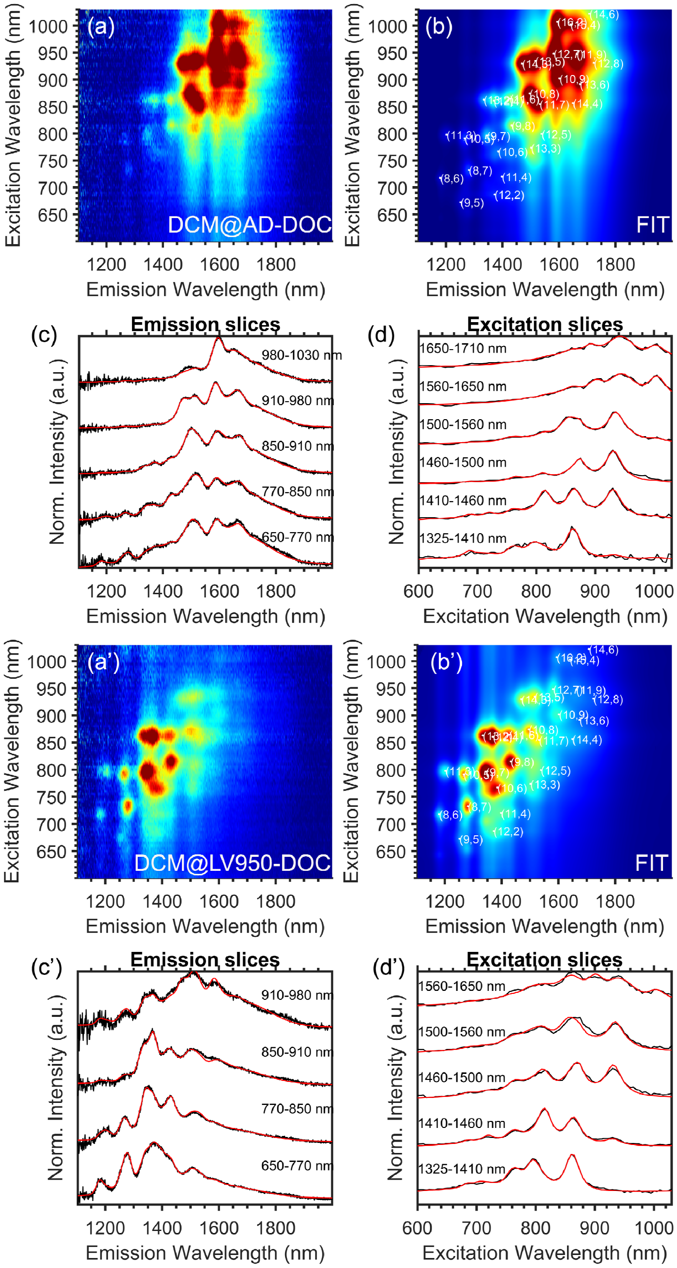

Figure S15: Experimental PLE maps and fits of DCM-filled AD (top 4 panels) and LV950 (bottom 4 panels) samples, fitted simultaneously with equal peak positions and line widths and varying amplitudes for each of the SWCNT peaks. Experimental (a, a’) and fitted (b, b’) PLE maps are presented, with fitted peak positions indicated by white dots and associated chiral indices. Integrated emission (c, c’) and excitation (d, d’) spectra of experimental (black) and fitted (red) PLE maps, integrated over the indicated wavelength ranges, highlight the excellent correspondence between experimental data and fit.

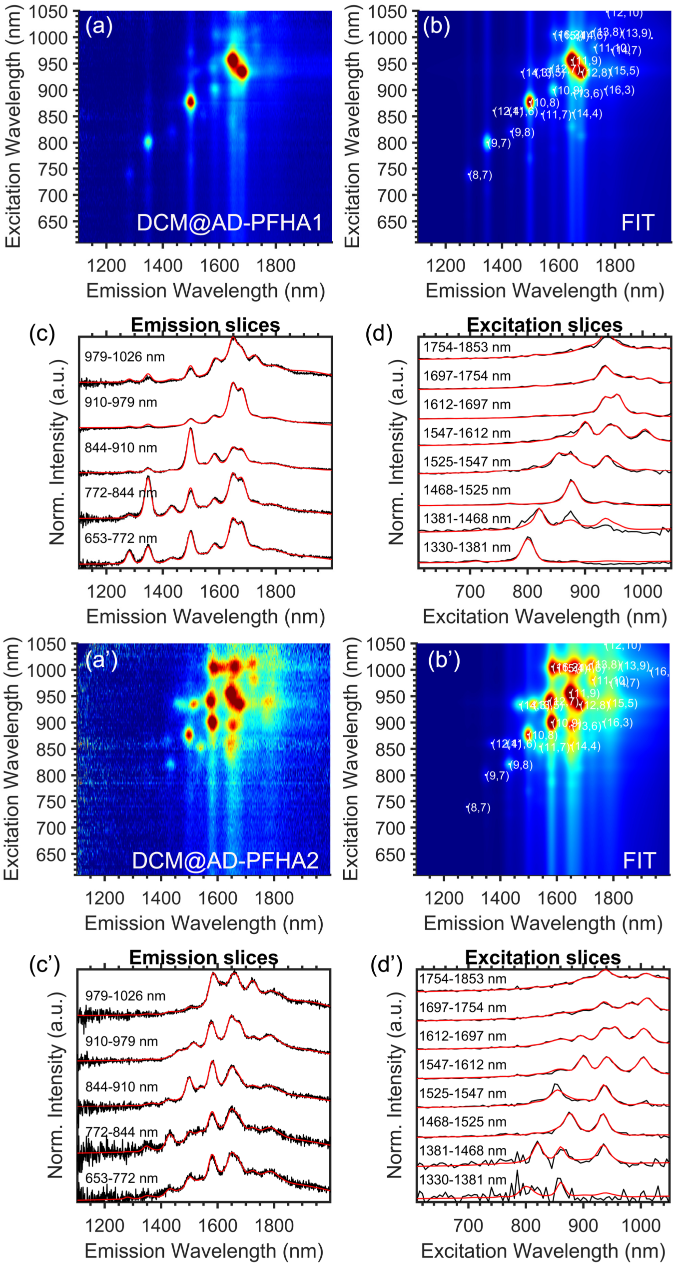

Figure S16: Experimental PLE maps and fits of DCM@AD-PFHA1 (top 4 panels) and DCM@AD-PFHA2 (bottom 4 panels) samples, fitted simultaneously with equal peak positions and line widths and varying amplitudes for each of the SWCNT peaks. Experimental (a, a') and fitted (b, b') PLE maps are presented, with fitted peak positions indicated by white dots and associated chiral indices. Integrated emission (c, c') and excitation (d, d') spectra of experimental (black) and fitted (red) PLE maps, integrated over the indicated wavelength ranges, highlight the excellent correspondence between experimental data and fit.

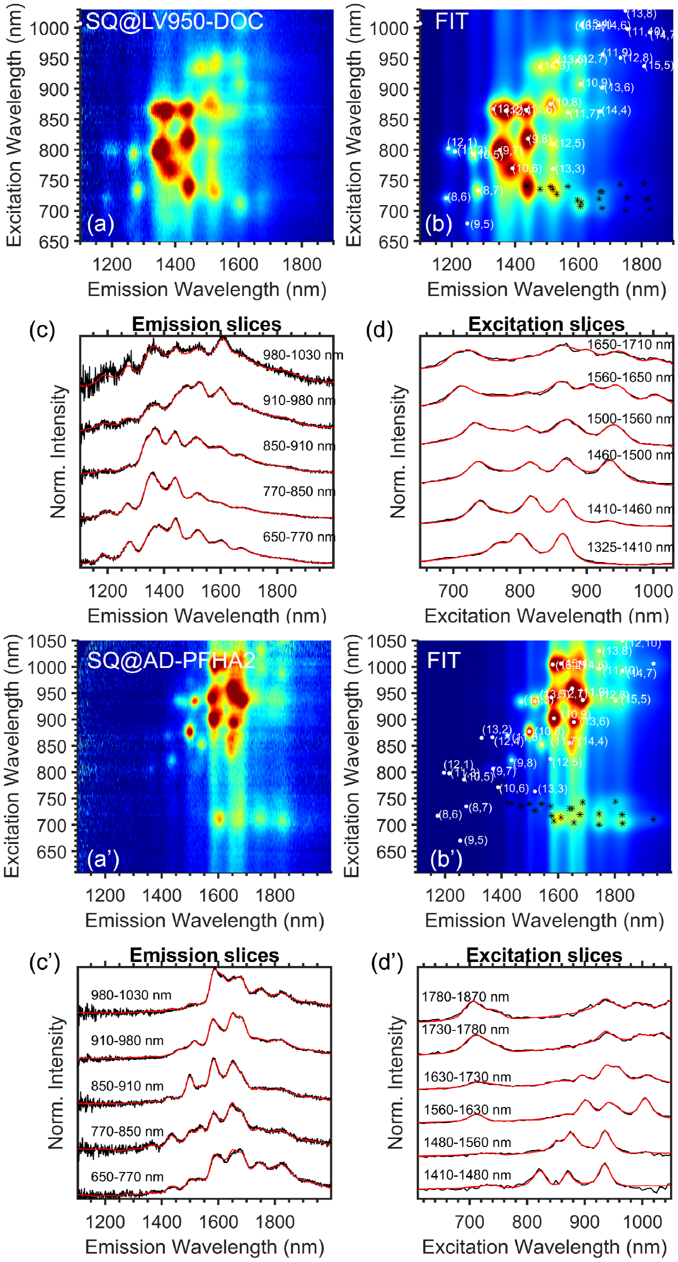

Figure S17: Experimental PLE maps and fits of SQ@LV950-DOC (top 4 panels) and SQ@AD-PFHA2 (bottom 4 panels) samples, fitted simultaneously (with SQ@AD-DOC, Figure 4 main text) with equal EET excitation positions and line widths and varying SWCNT peak positions, line widths and amplitudes. Experimental (a, a') and fitted (b, b') PLE maps are presented, with fitted peak positions indicated by white dots and associated chiral indices. Integrated emission (c, c') and excitation (d, d') spectra of experimental (black) and fitted (red) PLE maps, integrated over the indicated wavelength ranges, highlight the excellent correspondence between experimental data and fit.

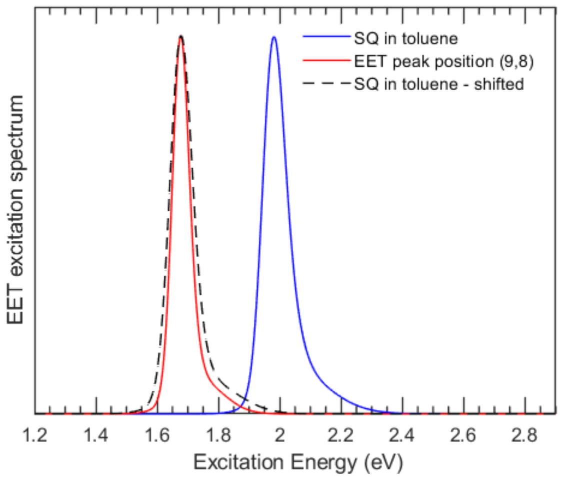

Figure S18: Fitted EET excitation spectrum (red) for the (9,8) chirality, as obtained from the 2D fit. To obtain this spectrum, we used the measured absorption spectrum of SQ in toluene and shifted (black dashed line) and scaled it to a 24% narrower line width. The scaling parameter is optimized during the fit. Note: the EET peak line width might change for different chiralities, but such variation was omitted from the fitting procedure to reduce the model complexity.

11. Time-resolved fluorescence of SQ in toluene

To determine the lifetime of the free dye, we dissolved SQ dye in a toluene. Figure S19 shows the time-resolved PL trace excited at 575 nm and integrated over the dye emission spectrum (590 – 760 nm). A convolution of a single exponential decay with the instrumental resolution function (IRF) provided a fit with a lifetime of (2.0 ± 0.1) ns, matching the decay extracted from fitting the transient absorption at the ground state bleach (Fig. 3b, main text).

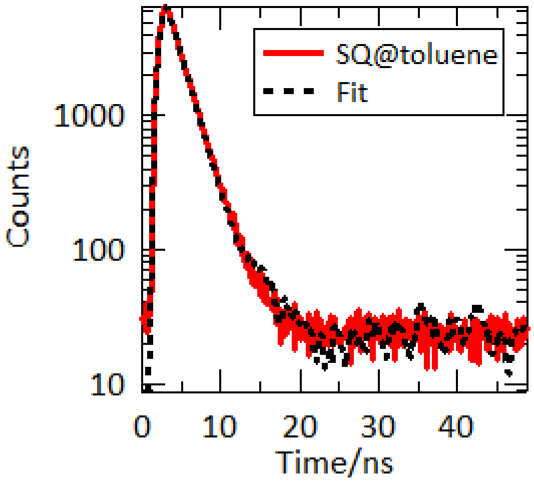

Figure S19: Time-resolved PL of SQ dissolved in toluene (red) and fit (black).

12. Excitation Energy Transfer Efficiency Estimation from TA

In the main text, we estimated the EET efficiency from the magnitude of the quenching of the SQ emission after encapsulation ($\phi_{EET} \gtrsim 99.999\%$) and from the changes in the TA kinetics for encapsulated SQ with respect to SQ freely dissolved in toluene ($\phi_{EET} \cong 99.99\ \%$). While both methods give a high precision, they rely on the assumption that the EET is the dominant factor for the observed changes in SQ PL and TA kinetics. Complementary to these approaches, we here extract the EET efficiency from the TA signal enhancement, where the EET can be directly identified.

To estimate the EET efficiency we model the S_{11} TA enhancement for SQ@SWCNT, which can be obtained from the number of absorbed photons by SQ encapsulated in s-SWCNTs tubes (N_{SQ}^{abs}) versus the number of absorbed photons by the s-SWCNTs tubes themselves (N_{SC}^{abs}) with

$$\begin{gathered} N_{SQ}^{abs} \propto \frac{2}{3}\left(\mathcal{A}_{SQ@NT}^{pu} - \mathcal{A}_{NT}^{pu}\right) \\ N_{SC}^{abs} \propto s\mathcal{A}_{NT}^{pu} \end{gathered} \qquad \text{(Eq. S1)}$$

where $\mathcal{A}_{i}^{pu}$is the *absorptance* (fraction of incident photons absorbed) of sample *i* at the pump wavelength, which can be obtained from the optical density (A_{i}^{pu}) measured in linear absorption by $\mathcal{A}_{i}^{pu} = 1 - 10^{-A_{i}^{pu}}$. The factor 2/3 accounts for the fact that only SQ molecules encapsulated in semiconducting SWCNTs can contribute to the S_{11} TA signal (assuming the usual random distribution of semiconducting and metallic SWCNTs). Similarly, the parameter *s* (0<*s*<1) is the fraction of absorbance in the DCM@SWCNT reference sample at the pump wavelength that is due to absorption by s-SWCNTs (i.e. excluding any contribution from metallic SWCNTs at this wavelength and excluding scattering), which is harder to estimate at this particular wavelength. The number of excitons resulting from EET (N_{SQ}^{exc}) and from direct absorption in S_{11} (N_{SC}^{exc}) is then

$$\begin{gathered} N_{SQ}^{exc} = \eta N_{SQ}^{abs} \\ N_{SC}^{exc} = N_{SC}^{abs} \end{gathered} \qquad \text{(Eq. S2)}$$

With η the unknown EET efficiency. The S_{11} TA enhancement, defined experimentally by

$$TA_{S11} = \frac{\Delta A_{SQ@NT}^{S11}}{\Delta A_{NT}^{S11}} \qquad \text{(Eq. S3)}$$

is then given by

$$TA_{S11} = \frac{N_{SC}^{abs} + \eta N_{SQ}^{abs}}{N_{SC}^{abs}} E_{GSA} \qquad \text{(Eq. S4)}$$

where

$$E_{GSA} = \frac{A^{S11}_{SQ@NT}}{A^{S11}_{NT}} \qquad \text{(Eq. S5)}$$

accounts for differences in ground state absorption magnitudes of S_{11} between the SQ@LV950-ATPE and DCM@LV950-ATPE reference sample. We must consider E_{GSA} because of differences in oscillator strength that may potentially arise from slightly different SWCNT distributions between the SQ and reference LV950-ATPE samples, from differences in environmental interactions experienced by samples (i.e. 'adventitious doping' by water/protons), and by any potential effects induced by electronic coupling between the S_{11} transitions of the SWCNTs and encapsulated SQ chromophores. Due to the difficulty in separating contributions of different s-SWCNTs, we integrated both the TA signal, $\Delta A_i^{S_{11}}$, and the ground state absorption, $A_i^{S_{11}}$, over the wavelength range 1385–1585 nm to get an estimation of the average EET efficiency for the probed s-SWCNTs.

Equating S3 and S4 and solving for η yields

$$\eta = \left(\frac{TA_{S11}}{E_{GSA}} - 1\right) \frac{s\mathcal{A}^{pu}_{NT}}{\frac{2}{3}\left(\mathcal{A}^{pu}_{SQ@NT} - \mathcal{A}^{pu}_{NT}\right)} \qquad \text{(Eq. S6)}$$

Alternatively, defining E_{pu} as the expected TA enhancement if η were 100%, Eq. S6 can also be rewritten as

$$\eta = \frac{{TA_{S11}}/{E_{GSA}} - 1}{E_{pu} - 1} \qquad \text{(Eq. S7)}$$

For the data in Fig. 3, $TA_{S11} = 1.42$, $E_{GSA} = 1.19$, and $E_{pu} = 1.31$, giving an EET efficiency η = 64% with $s = 1$.

To check the internal consistency of this approach, we also performed TA measurements on slightly different samples, but exciting both at 740nm (SQ absorption) and at 850nm, outside the SQ absorption band, hence only exciting directly into the SWCNTs S_{22} transition, where thus no EET enhancement is expected. Figure S20 displays the data exciting at 740 nm (SQ excitation) and shows how E_{pu}, E_{GSA}, and TA_{S11} were obtained. For this data, $TA_{S11} = 1.24$, E_{GSA} = 0.78, and $E_{pu} = 1.65$. For $s = 0.71$ this gives η = 90%; for s = 0.79 η = 100%. These estimates for s are compatible with previous reports on mixtures of m- and s-SWCNTS, as demonstrated in the supporting information of Mistry et al.[3]

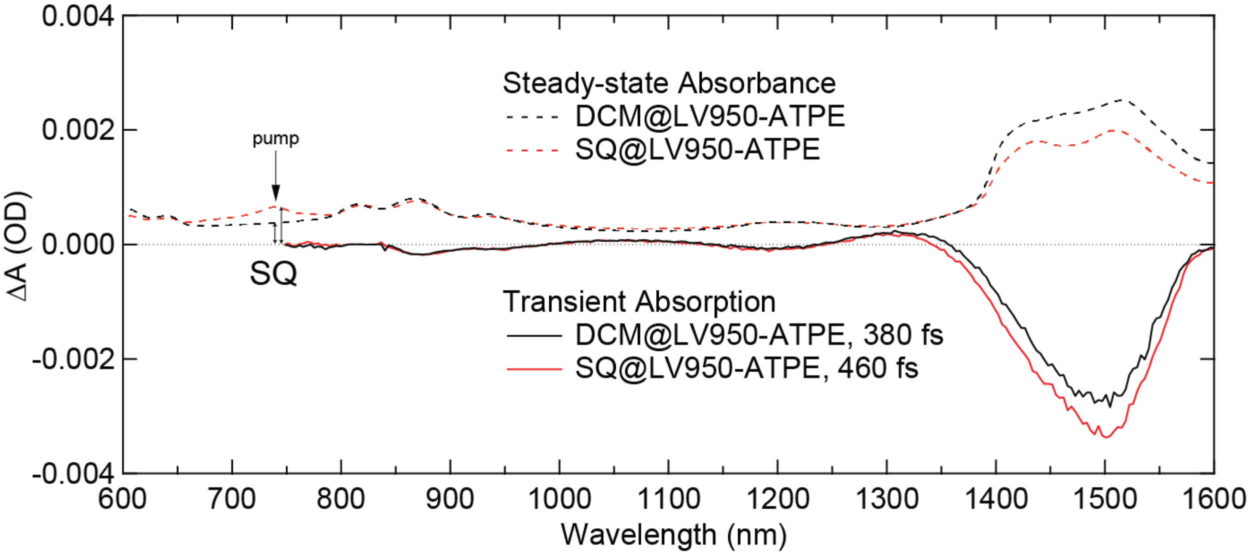

Figure S20: Linear absorption (dotted lines) and TA signals (solid lines) for DCM@LV950-ATPE and SQ@LV950-ATPE samples for an excitation wavelength of 740 nm (in the SQ absorption band).

For comparison, exciting near the S_{22} we do not have to account for SQ absorption, and the TA_{11} signal should be linearly proportional to the ground state absorption (E_{GSA}). Fig. S21 shows linear absorption and TA data for pumping near the S_{22} (850 nm). Near the S_{22}, the OD is nearly matched ($E_{pu} \approx 0.93$) and $TA_{S11}/E_{GSA} = 0.79/0.78 = 1.01$, in excellent agreement with expectations (no EET enhancement when exciting outside the SQ absorption band).Hence, although large uncertainties are associated with this estimation (e.g. also on the parameter *s*), the resulting efficiency estimation is in agreement with a (near) quantitative EET.

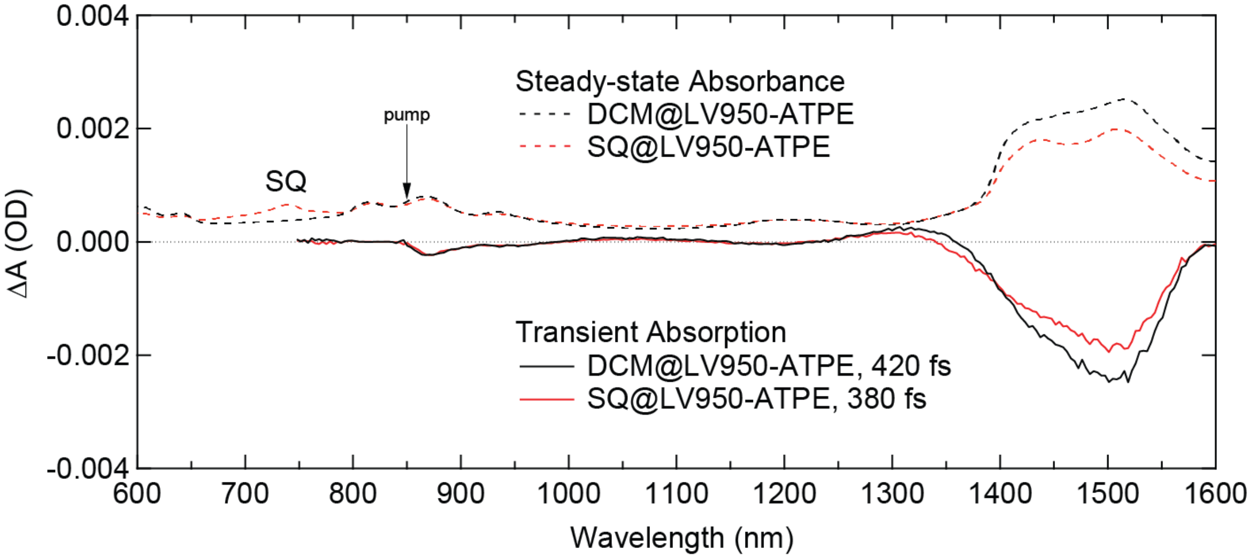

Figure S21: Linear absorption (dotted lines) and TA signals (solid lines) for DCM@LV950-ATPE and SQ@LV950-ATPE samples for an excitation wavelength of 850 nm (in SWCNT S_{22} transition, outside SQ absorption band).

13. TA spectroscopy of SQ@AD-PFHA1 samples

We also performed TA spectroscopy on s-SWCNTs extracted with PFHA1 to eliminate contributions from metallic tubes. Separation of contributions from individual species was complicated by both the wider distribution and greater spectral overlap of various s-SWCNTs. However, very fast (200 ±10) fs EET and a slower picosecond decay were still observed for the SQ ground state bleach (GSB) in these samples (Fig. S22c), implying that the slow components in the SQ@LV950-ATPE SWCNTs were not due to EET to metallic species.

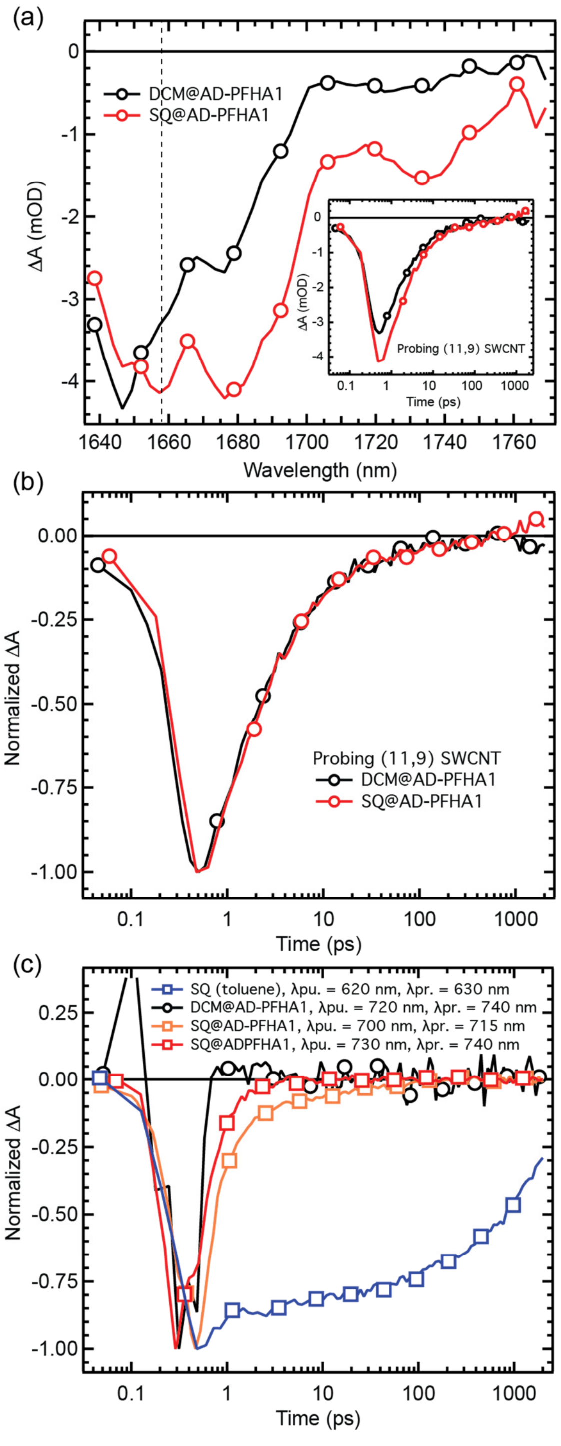

Figure S22: TA spectroscopy and kinetics of the SQ@AD-PFHA1 samples (a) The early time (~500 fs) transient spectra probed in an IR region covering a portion of the S_{11} exciton envelope – the inset shows dynamics of the GSB signal at 1657 nm after photoexcitation at 720 nm. (b) Normalized dynamics for the data shown in panel (a). (c) Dynamics associated with the GSB of the SQ dye, after excitation at various wavelengths – the dynamics for isolated SQ dye in toluene are also shown for reference.

14. Comparison of SQ and CNT Kinetics in SQ@LV950-ATPE

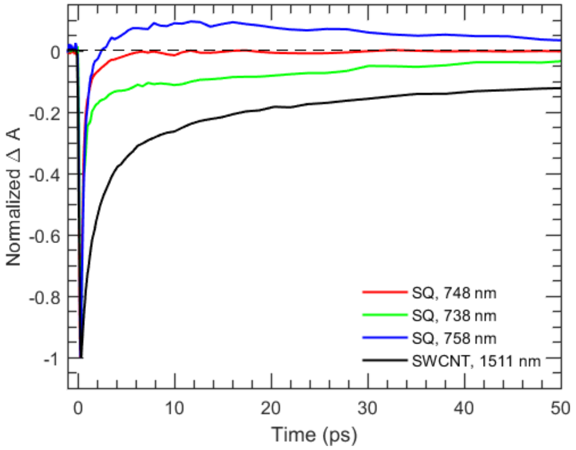

Figure S23: TA kinetics of SQ@LV950-ATPE sample directly comparing the SWCNT GSB recovery to the SQ GSB recovery.

Fig. S23 compares the LV950-ATPE GSB recovery of the SWCNTs with that of the encapsulated SQ dyes. The derivative-like TA signal (blue and green curves in Fig. S23, and highlighted in Fig. 4 in the main text) has a decay component of ca. 35 ps, which may also be present in the GSB recovery of the SWCNTs superimposed on a much slower (~ns) component. The combination of similar decay time scales in SQ and SWCNT GSB recoveries and the fact that the derivative-like TA signal points at a red-shift of the SQ ground-state absorption, is consistent with a Stark effect induced by the optically generated charge carriers in the SWCNTs. While different explanations have been provided in literature for the ~ns decay component in the SWCNTs' GSB, e.g. triplet excitons[4] or phonon thermalisation,[5] both of them are in agreement with the fact that this component is not observed in the SQ GSB. Although we cannot rule out any other mechanisms, the Stark effect yields the most plausible explanation for the origin of the ca. 35ps derivative-like TA signal.

References

(1) Cornelissen-Gude, C.; Rettig, W.; Lapouyade, R. *The Journal of Physical Chemistry A* **1997**, *101*, 9673.

(2) Cambré, S.; Campo, J.; Beirnaert, C.; Verlackt, C.; Cool, P.; Wenseleers, W. *Nature nanotechnology* **2015**, *10*, 248.

(3) Mistry, K. S.; Larsen, B. A.; Blackburn, J. L. *ACS nano* **2013**, *7*, 2231.

(4) Stich, D.; Späth, F.; Kraus, H.; Sperlich, A.; Dyakonov, V.; Hertel, T. *Nature Photonics* **2014**, *8*, 139.

(5) Koyama, T.; Yoshimitsu, S.; Miyata, Y.; Shinohara, H.; Kishida, H.; Nakamura, A. *The Journal of Physical Chemistry C* **2013**, *117*, 20289.